scientific reports

Check for updates

OPEN

Exceptional lines and higher-order exceptional points enabled by uniform loss

Fanghu Feng, Neng Wang✉ & Guo Ping Wang✉

This study theoretically investigates the realization of exceptional points (EPs) in space-time invariant Lorentz dispersive media with uniform loss, which contrasts sharply with conventional approaches that rely on spatial or temporal differential losses. Using the derived full and reduced Hamiltonians, we reveal that uniform loss in Lorentz dispersive media not only introduces attenuation to the eigenmodes of the lossless medium but also enables two distinct types of non-Hermitian couplings: reciprocal and non-reciprocal. Both coupling mechanisms independently contribute to the emergence of EPs. The EPs manifest as exceptional lines (ELs) in the parameter space, and a fourth-order EP (EP4) is formed when three ELs intersect at a single point. Remarkably, at the EP4, all eigenmodes exhibit maximum optical chirality density, presenting potential applications such as chiral sorting. Our findings provide valuable insights into the mechanisms underpinning the formation of EPs.

In non-Hermitian systems, exceptional points (EPs) emerge when two or more eigenvalues and their corresponding eigenvectors coalesce[1]. The unique mathematical and physical properties have spurred extensive exploration of EPs across various disciplines, including quantum systems[2,3], acoustic systems[4–8], circuit systems[9,10], and optical systems[11–18]. In optics, the abrupt degeneracy of eigenmodes near EPs gives rise to a host of intriguing phenomena and applications. These include advancements in laser technology[19,20], exceptional topological structures[21–25], and enhanced sensitivity for sensing applications[26].

Second-order EPs (EP2s) are initially proposed in systems obeying parity-time (PT) symmetry[27–30]. However, precisely balancing gain and loss in optics remains technically challenging. Later, alternative approaches, such as employing two resonators with differing losses, have been proposed[31,32]. Compared with EP2s, higher-order EPs exhibit more fascinating properties, driving interest in their realizations[33–39]. In conventional approaches, achieving high-order EPs generally requires coupling three or more resonators and meticulously fine-tuning the loss parameters of each resonator. A recent study has suggested that a uniform loss structure can enable EPs[40]. However, this approach still requires spatially nonuniform configurations and the EPs are limited to the second-order.

Diverging from conventional approaches that rely on spatial or temporal variations in loss, this work achieves EPs by introducing uniform loss to space-time invariant Lorentz dispersive media. The system's Hamiltonian is formulated using Maxwell's equations and the Lorentz dispersion model, with theoretical investigations focusing on the interactions between plane wave modes through reduced Hamiltonians. The results reveal that EPs emerge from non-Hermitian couplings induced by the uniform loss. In addition to conventional reciprocal couplings, this study reveals the presence of non-reciprocal couplings between plane wave modes with different polarization states. EPs in this system manifest as exceptional lines (ELs) in the parameter space, making them inherently robust. When three ELs intersect, they form a fourth-order EP (EP4), where all eigenmodes collapse into a single mode. Remarkably, the EP4 is characterized by maximum optical chirality density, highlighting its potential for applications such as chiral sorting.

Methods

Modeling and the Hamiltonian of Lorentz dispersive medium

Consider an isotropic, homogeneous and nonmagnetic (relative permeability is unity) Lorentz dispersive medium, the relative permittivity at frequency ω is given by:

$$\varepsilon(\omega) = 1 + \frac{\omega_p^2}{\omega_0^2 + i\gamma\omega - \omega^2}, \tag{1}$$

China State Key Laboratory of Radio Frequency Heterogeneous Integration, College of electronics and Information Engineering, Shenzhen University, Shenzhen 518060, China. ✉email: nwang17@szu.edu.cn; gpwang@szu.edu.cn

where ω_p, ω_0 are the plasmon and resonant frequencies, and γ denotes the damping rate. Regarding this medium, the Maxwell's equations and the differential equation for the polarization charge $\mathbf{P}$ are expressed as:

$$\nabla \times \mathbf{E} = -\mu_0 \frac{\partial \mathbf{H}}{\partial t}, \tag{2}$$

$$\nabla \times \mathbf{H} = \varepsilon_0 \frac{\partial \mathbf{E}}{\partial t} + \frac{\partial \mathbf{P}}{\partial t}, \tag{3}$$

$$\frac{\partial^2 \mathbf{P}}{\partial t^2} + \gamma \frac{\partial \mathbf{P}}{\partial t} + \omega_0^2 \mathbf{P} = \varepsilon_0 \omega_p^2 \mathbf{E}, \tag{4}$$

where $\mathbf{E}, \mathbf{H}$ are the electric field, magnetic field, respectively, and ε_0, μ_0 are the relative permittivity and permeability in the vacuum. For simplicity, hereafter, we just let $\varepsilon_0 = \mu_0 = c = 1$, where c is the speed of light in vacuum. Introducing an identity equation:

$$i\frac{\partial}{\partial t}\mathbf{P} = i\frac{\partial \mathbf{P}}{\partial t}, \tag{5}$$

Equations (2–5) can be rewritten into a Schrodinger-like eigenvalue equation as[41,42]:

$$i\frac{\partial}{\partial t}\begin{pmatrix} \mathbf{E} \\ \mathbf{H} \\ \mathbf{P} \\ \frac{\partial \mathbf{P}}{\partial t} \end{pmatrix} = \begin{pmatrix} 0 & i\nabla\times & 0 & -i\overleftrightarrow{I} \\ -i\nabla\times & 0 & 0 & 0 \\ 0 & 0 & 0 & i\overleftrightarrow{I} \\ i\omega_p^2\overleftrightarrow{I} & 0 & -i\omega_0^2\overleftrightarrow{I} & -i\gamma\overleftrightarrow{I} \end{pmatrix} \begin{pmatrix} \mathbf{E} \\ \mathbf{H} \\ \mathbf{P} \\ \frac{\partial \mathbf{P}}{\partial t} \end{pmatrix}, \tag{6}$$

where $\overleftrightarrow{I}$ is the identity matrix. Since the medium is isotropic, the eigenmodes are linearly polarized. Without loss of generality, we assume that the incident wave is a plane wave, and the electromagnetic field is linearly polarized along the x direction ($\mathbf{E} = E_x\hat{x}$) while propagating along the z direction ($\mathbf{k} = k\hat{z}$). Then, Eq. (6) can be reduced into:

$$i\frac{\partial}{\partial t}\vec{\psi} = \hat{H}\vec{\psi}, \tag{7}$$

where $\vec{\psi} = (E_x, H_y, P_x, \partial P_x/\partial t)^T$ denotes the state vector,

$$\hat{H} = \hat{H}_0 + \hat{H}_r = \begin{pmatrix} 0 & k & 0 & -i \\ k & 0 & 0 & 0 \\ 0 & 0 & 0 & i \\ i\omega_p^2 & 0 & i\omega_0^2 & 0 \end{pmatrix} + \begin{pmatrix} 0 & 0 & 0 & 0 \\ 0 & 0 & 0 & 0 \\ 0 & 0 & 0 & 0 \\ 0 & 0 & 0 & i\gamma \end{pmatrix}, \tag{8}$$

represents the full Hamiltonian, $\hat{H}_0$ denotes the unperturbed Hamiltonian and $\hat{H}_r$ is the non-Hermitian perturbation matrix.

In the absence of perturbation ($\gamma = 0$), $\hat{H}_r$ is null, the eigenfrequencies of this lossless medium are calculated as:

$$\omega_{1,2,3,4} = -\sqrt{\frac{K_1 - K_0}{2}}, \sqrt{\frac{K_1 - K_0}{2}}, -\sqrt{\frac{K_1 + K_0}{2}}, \sqrt{\frac{K_1 + K_0}{2}}, \tag{9}$$

where $K_1 = k^2 + \omega_0^2 + \omega_p^2$, $K_0 = \sqrt{K_1^2 - 4k^2\omega_0^2}$. And the corresponding eigenvectors are given by $\vec{v}_i$, of which the expressions are not shown here for brevity. Note that K_1 and K_0 are both positive real and $K_1 > K_0$ when k is real, ensuring the realities of $\omega_{1,2,3,4}$. Therefore, $\hat{H}_0$ is a pseudo-Hermitian matrix when k is purely real. $\omega_{1,2}$ ($\omega_{3,4}$) are corresponding to the same polarization mode but propagates along the backward ($-z$) and forward ($+z$) directions, respectively.

We now introduce the rotation matrix which is constructed by the eigenvectors of $\hat{H}_0$:

$$\hat{R} = (\vec{v}_1, \vec{v}_2, \vec{v}_3, \vec{v}_4). \tag{10}$$

$\vec{v}_i$characterize the four linearly polarized plane wave modes in the lossless limit. Imposing the following similarity transformation:

$$\hat{H}' = \hat{R}^{-1} \cdot \hat{H} \cdot \hat{R}. \tag{11}$$

In the transformed basis, the unperturbed Hamiltonian is diagonalized as: $\hat{H}_0' = \hat{R}^{-1} \cdot \hat{H}_0 \cdot \hat{R} = diag\{\omega_1, \omega_2, \omega_3, \omega_4\}$, while the non-Hermitian perturbation matrix becomes

$$\hat{H}_r' = \hat{R}^{-1} \cdot \hat{H}_r \cdot \hat{R} = i\gamma \begin{pmatrix} m & m & m & m \\ m & m & m & m \\ n & n & n & n \\ n & n & n & n \end{pmatrix}, \tag{12}$$

where $m = -(K_2 + K_0)/(4K_0)$, $n = (K_2 - K_0)/(4K_0)$ with $K_2 = k^2 - \omega_0^2 - \omega_p^2$.Therefore, the full Hamiltonian in the new basis is expressed as:

$$\hat{H}' = \begin{pmatrix} \omega_1 + im\gamma & im\gamma & im\gamma & im\gamma \\ im\gamma & \omega_2 + im\gamma & im\gamma & im\gamma \\ in\gamma & in\gamma & \omega_3 + in\gamma & in\gamma \\ in\gamma & in\gamma & in\gamma & \omega_4 + in\gamma \end{pmatrix}. \tag{13}$$

Results

Exceptional lines and higher-order exceptional point

To explore the band dispersions under various parameter modulations, we present the complex eigenfrequencies in the three-dimensional parameter space (ω_p, γ, k) by the full Hamiltonian $\hat{H}'$ in Eq. (13). When we vary ω_p, γ and fix $k = \omega_0/c$, the EPs evolve continuously in the parameter space and form ELs. As shown in Figs. 1a and b, two ELs of the second order (i.e., $EL2_1$, $EL2_2$) lie in the two-dimensional (2D) parameter space (ω_p, γ). These two EL2s intersect with each other at the point q (red circles in Fig. 1a and b). This point is a fourth-order EP (EP4).

For $EL2_{1,2}$ which is at $k = \omega_0/c$, using Eq. (13), we can obtain four eigenfrequencies as follows:

$$\tilde{\omega}_1 = \frac{1}{4}\left(i\gamma - \sqrt{4\omega_p^2 - \gamma^2} - \sqrt{-2\gamma^2 + 4\left(4\omega_0^2 + \omega_p^2\right) - 2i\gamma\sqrt{4\omega_p^2 - \gamma^2}}\right), \tag{14a}$$

$$\tilde{\omega}_2 = \frac{1}{4}\left(i\gamma - \sqrt{4\omega_p^2 - \gamma^2} + \sqrt{-2\gamma^2 + 4\left(4\omega_0^2 + \omega_p^2\right) - 2i\gamma\sqrt{4\omega_p^2 - \gamma^2}}\right), \tag{14b}$$

$$\tilde{\omega}_3 = \frac{1}{4}\left(i\gamma + \sqrt{4\omega_p^2 - \gamma^2} - \sqrt{-2\gamma^2 + 4\left(4\omega_0^2 + \omega_p^2\right) - 2i\gamma\sqrt{4\omega_p^2 - \gamma^2}}\right), \tag{14c}$$

$$\tilde{\omega}_4 = \frac{1}{4}\left(i\gamma + \sqrt{4\omega_p^2 - \gamma^2} + \sqrt{-2\gamma^2 + 4\left(4\omega_0^2 + \omega_p^2\right) - 2i\gamma\sqrt{4\omega_p^2 - \gamma^2}}\right). \tag{14d}$$

The eigenfrequecies are complex generally. Here, we use the tilde symbols to distinguish with real valued $\omega_{1,2,3,4}$ in the lossless limit. According to Eq. (14), $\tilde{\omega}_1(\tilde{\omega}_2)$ and $\tilde{\omega}_3(\tilde{\omega}_4)$ degenerate when $4\omega_p^2 - \gamma^2 = 0$. Then, the eigenfrequencies are simplified to:

$$\tilde{\omega}_1 = \tilde{\omega}_3 = \frac{1}{4}\left(i\gamma - \sqrt{16\omega_0^2 - \gamma^2}\right), \tag{15a}$$

$$\tilde{\omega}_2 = \tilde{\omega}_4 = \frac{1}{4}\left(i\gamma + \sqrt{16\omega_0^2 - \gamma^2}\right). \tag{15b}$$

Therefore, the preconditions of forming an EP2 at $EL2_{1,2}$ are $k = \omega_0/c, \omega_p = 0.5\gamma$. According to Eq. (15), $EL2_1$ ($EL2_2$) corresponds to the intersection line of $\tilde{\omega}_2$ and $\tilde{\omega}_4$ ($\tilde{\omega}_1$and $\tilde{\omega}_3$) sheets, with the real eigenfrequencies nonzero when $\gamma < 4\omega_0$ and zero when $\gamma \geqslant 4\omega_0$. At $EL2_{1,2}$, the eigenfrequencies satisfy:

$$\mathrm{Re}[\tilde{\omega}_1] = \mathrm{Re}[\tilde{\omega}_3] = -\mathrm{Re}[\tilde{\omega}_2] = -\mathrm{Re}[\tilde{\omega}_4], \tag{16a}$$

$$\mathrm{Im}[\tilde{\omega}_i] = \frac{\gamma}{4}, i = 1, 2, 3, 4. \tag{16b}$$

Moreover, according to Eq. (15), the four eigenfrequencies coalesce to a single point (EP4) when $\gamma = 4\omega_0$, with the eigenfrequencies degenerate to

$$\mathrm{Re}[\tilde{\omega}_i] = 0, \mathrm{Im}[\tilde{\omega}_i] = \omega_0, i = 1, 2, 3, 4. \tag{17}$$

Therefore, the preconditions for the emergence of EP4 are $k = \omega_0/c, \omega_p = 0.5\gamma, \gamma = 4\omega_0$.

In summary, introducing uniform loss ($\gamma > 0$) into the Lorentzian medium breaks Hermiticity, enabling non-Hermitian couplings among the linearly polarized plane wave modes. As illustrated in Fig. 1e–f, the non-Hermitian couplings drive the coalescence of eigenfrequencies, resulting in the emergence of EPs.

The order of an EP can be rigorously determined through perturbation analysis by evaluating the splitting of eigenfrequencies under small parameter variations. Near an EP of order N, the eigenfrequencies' splitting $\Delta\omega = \omega - \omega_{EP}$, where ω_{EP} is the eigenfrequency precisely at the EP, exhibits the following power-law dependence[26,33]:

$$|\Delta\omega| = \epsilon^{1/N}, \tag{18}$$

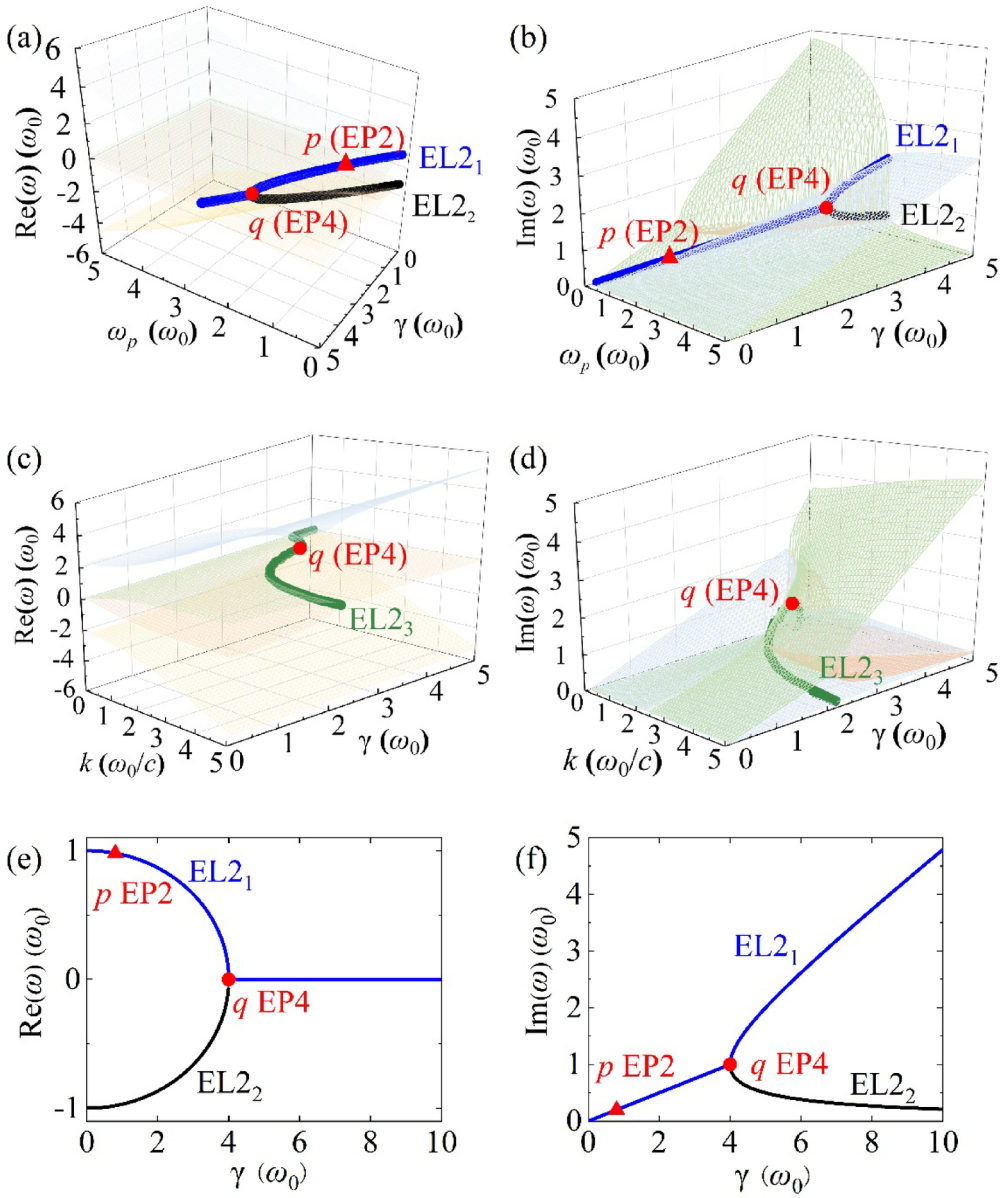

Fig. 1. Exceptional lines (ELs) and higher-order exceptional point (EP) in the parameter space. The four sheets of different colors represent the four bands. The bule, black and green curves are three intersection lines among these sheets, denoting exceptional lines of the second order (EL2s), and are labeled as $EL2_1$, $EL2_2$, and $EL2_3$, respectively. We fix $k = \omega_0/c$ in panels (**a**) and (**b**), and fix $\omega_p = 2\omega_0$ in panels (**c**) and (**d**). The red triangle p ($\omega_p = 0.5\gamma = 0.4\omega_0, k = \omega_0/c$) is an arbitrary chosen point on $EL2_1$. The red circle q ($\omega_p = 0.5\gamma = 2\omega_0, k = \omega_0/c$) depicts a fourth-order exceptional point (EP4), which is the crossing point of the three EL2s. (**e**) Real and (**f**) imaginary parts of band dispersions with $\omega_p = 0.5\gamma$ and $k = \omega_0/c$.

where ϵ represents any deviation in k, ω_p or γ from their corresponding values at the EP. The derivation of Eq. (18) can be found in Ref. 26. As shown in Fig. 2, the log-log plots of eigenfrequencies' splitting $|\Delta\omega|$ versus the deviation of damping rate $\Delta\gamma$ around point$p$ and point q are displayed by orange and blue lines, respectively. Point p is an arbitrary chosen point on EL2. The slop of the orange line is approximately 0.5, confirming that point p is an EP2. Conversely, the slope of the blue line is approximately 0.25, verifying that the order of point q is indeed of four.

Optical chirality density

In general, EPs are associated with singular physical phenomena. In this work, we explore the optical chirality of the eigenstates in the vicinity of the EPs. When loss is introduced in the Lorentz dispersive medium, the electromagnetic fields usually exhibit optical chirality[43]. Optical chirality density is a physics quantity that generally characterizes optical chiral interactions. The expression of normalized optical chirality density χ is defined as[44,45]:

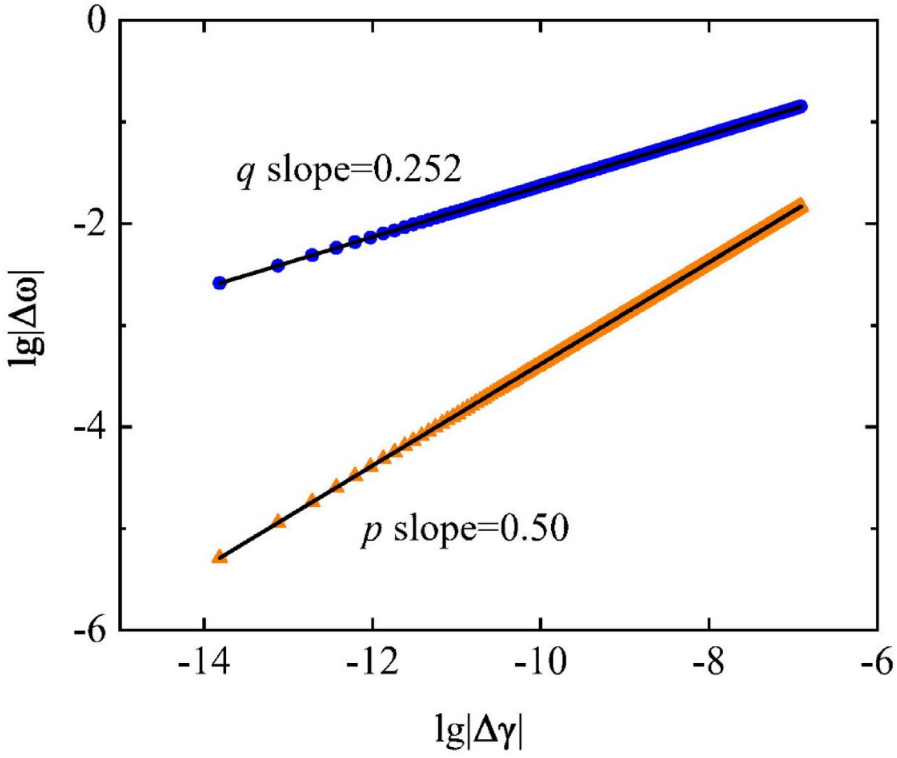

Fig. 2. Log-log plots of the eigenfrequency splitting $|\Delta\omega|$ as functions of the damping rate deviation $|\Delta\gamma|$ around point p (orange triangles) and point q (blue circles). The black solid lines represent linear fitting curves, with the respective slopes indicated.

$$\chi = -\frac{\frac{1}{2}\,\mathrm{Im}\,(E_x^* \cdot H_y)}{\frac{1}{4}\left(|E_x|^2+|H_y|^2\right)}. \tag{19}$$

Combining Eqs. (7) and (19), the optical chirality densities of the four eigenmodes around point p and point q are calculated, and plotted in Fig. 3a and b, respectively. The electric field (E_x) and magnetic field (H_y) used to calculate optical chirality density are derived from the eigenvectors of the full Hamiltonian $\hat{H}$. According to the definition of $\vec{\psi}$, $E_x$and H_y are corresponding to the first and second elements of the eigenvectors.

The optical chirality density χ_i is associated with the eigenfrequency ω_i. It is evident that the EPs are singular points for the optical chirality densities. When approaching point p (EP2), the normalized optical chirality densities rapidly converge to a median value ~ 0.2, as shown in Fig. 3a. The optical chirality densities are doubly degenerate because the associated eigenstates are just the counter-propagating mode pairs. In contrast, at point p (EP4), the normalized optical chirality densities of all eigenstates also rapidly converge and reach the maximum value of 1. This peak value highlights the maximum asymmetry, making it a useful tool in distinguishing the handedness of chiral molecules, with potential applications in pharmaceutics and synthetic chemistry.

Furthermore, we calculate the optical chirality density under parametric modulation of both γ and k, as illustrated in Fig. 3c. Our results show that the optical chirality density can be continuously tuned from its maximum value of 1 to 0. Additionally, as shown in Fig. 3d, varying γ within the range $0 < \gamma < 4\omega_0$ induces a linear modulation of optical chirality density from 0 to 1, demonstrating a linear tuning regime enabled by the uniform loss.

Discussion

To further analyze the mechanisms underpinning the formation of EPs, let us pay attention to the first pair of counter-propagating plane wave modes (i.e., ω_1, ω_2) in Eq. (14). According to the expression of $\hat{H}'$, the dispersion relations of this pair of counter-propagating plane wave modes can be approximated by the following 2×2 reduced Hamiltonian when $\omega_{3,4}$ are far away from ω_1, ω_2:

$$\hat{H}_{red} = \begin{pmatrix} \omega_1 + im\gamma & im\gamma \\ im\gamma & \omega_2 + im\gamma \end{pmatrix}. \tag{20}$$

Obviously, Eq. (20) reveals that the spatially uniform damping rate ($\gamma \neq 0$) not only creates an equal loss to the forward and backward propagating modes, (i.e., $im\gamma$ to ω_1 and ω_2), but also generates a non-Hermitian ($\hat{\Delta} = (0, im\gamma; im\gamma, 0)$, $\hat{\Delta} \neq \hat{\Delta}^\dagger$) and reciprocal ($\hat{\Delta} = \hat{\Delta}^T$) coupling between these two modes. According

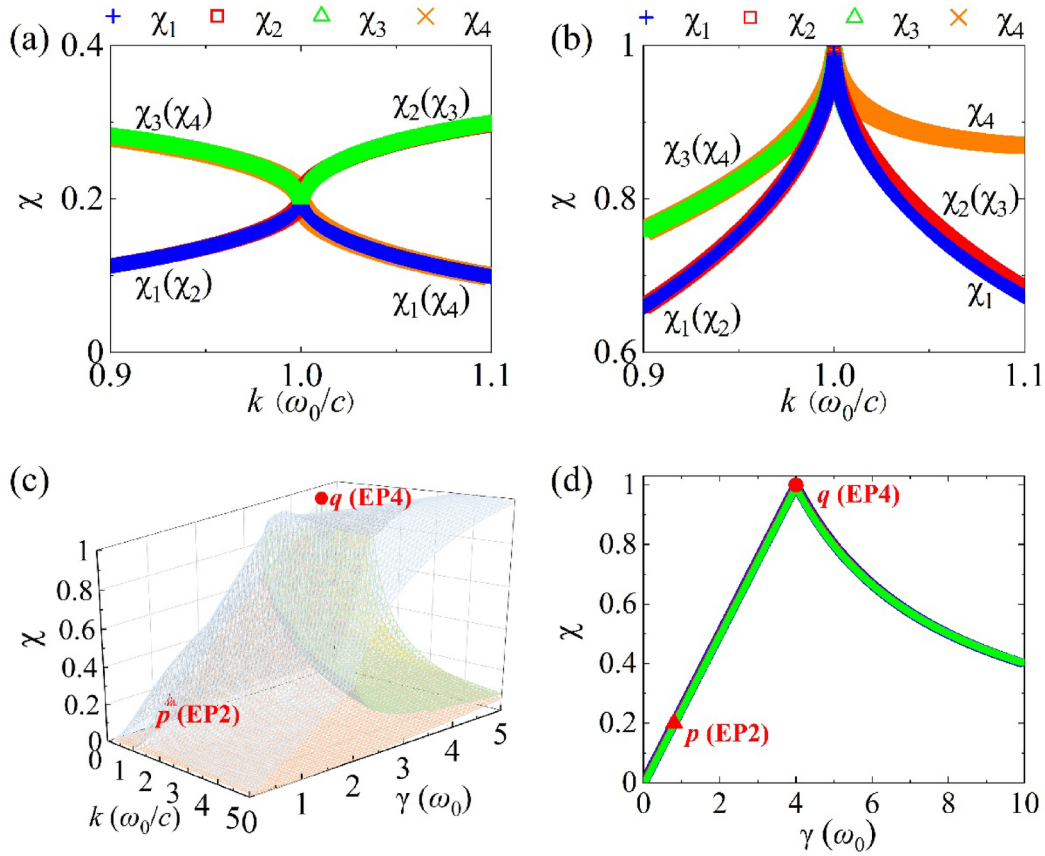

Fig. 3. Optical chirality densities of the eigenmodes around (**a**) triangle p (EP2) and (**b**) circle q (EP4) from Fig. 1, both at $k = \omega_0/c$. Parameters used are (**a**) $\omega_p = 0.5\gamma = 0.4\omega_0$, (**b**) $\omega_p = 0.5\gamma = 2\omega_0$. (**c**) Optical chirality densities in the γ-k parameter space, where four eigenmodes (colored sheets) exhibit distinct optical chiral densities. (**d**) Loss-controlled optical chiral density modulation under $k = \omega_0/c$, $\omega_p = 0.5\gamma$.

to Eq. (20), an EP will appear when $\gamma = \sqrt{8K_0^2(K_1 - K_0)}/(K_2 + K_0)$. Therefore, EPs can be enabled by spatially uniform loss in the Lorentz dispersive medium, originated from the non-Hermitian coupling. This is in sharp contrast with traditional EP engineering based on the following type of Hamiltonian[13,14]:

$$\hat{H}_{tra} = \begin{pmatrix} \omega_1 + i\gamma_1 & g \\ g & \omega_2 + i\gamma_2 \end{pmatrix}, \tag{21}$$

where spatially differential losses ($\gamma_1 \neq \gamma_2$) are necessary for a Hermitian and reciprocal coupling.

Similarly, the interaction between different polarization modes but propagating along the same direction (e.g., ω_1, ω_3) can be approximated by the following reduced Hamiltonian:

$$\hat{H}'_{red} = \begin{pmatrix} \omega_1 + im\gamma & im\gamma \\ in\gamma & \omega_3 + in\gamma \end{pmatrix}. \tag{22}$$

In this scenario, the spatially uniform damping rate contributes unequal losses to the two modes and generates a non-Hermitian and nonreciprocal coupling. Importantly, EP can also be induced by the spatially uniform loss according to Eq. (22).

There are two reasons for employing the 2×2 reduced Hamiltonian: first it provides a clearer physical representation of non-Hermitian couplings, and second it offers a direct way to compare with the Hamiltonian (i.e., Eq. (21)) in traditional EP2 engineering. While the full 4×4 Hamiltonian is mathematically rigorous, its complexity makes it less practical for gaining an intuitive understanding of eigenmode interactions. Based on the reduced Hamiltonian, we demonstrate that the EP2 can generally be classified into two types according to the forms of non-Hermitian couplings. Moreover, our reduced Hamiltonian reveals that the EP2s are originated from a distinguish mechanism.

To illustrate the applicability of the reduced Hamiltonian (e.g., Eq. (20)), we compare the dispersion relation $\tilde{\omega}_{1,2}(k)$ obtained from the reduced Hamiltonian with the rigorous results obtained by the full Hamiltonian $\hat{H}'$ in Fig. 4 for the given ω_p and γ. The eigenfrequencies are complex across the entire band due to the inherent loss in the medium, which introduces imaginary components to the frequencies. As illustrated in Fig. 4a–b, due to the ignoring of interactions with the other two bands ($\tilde{\omega}_{3,4}(k)$), the band diagram obtained from the

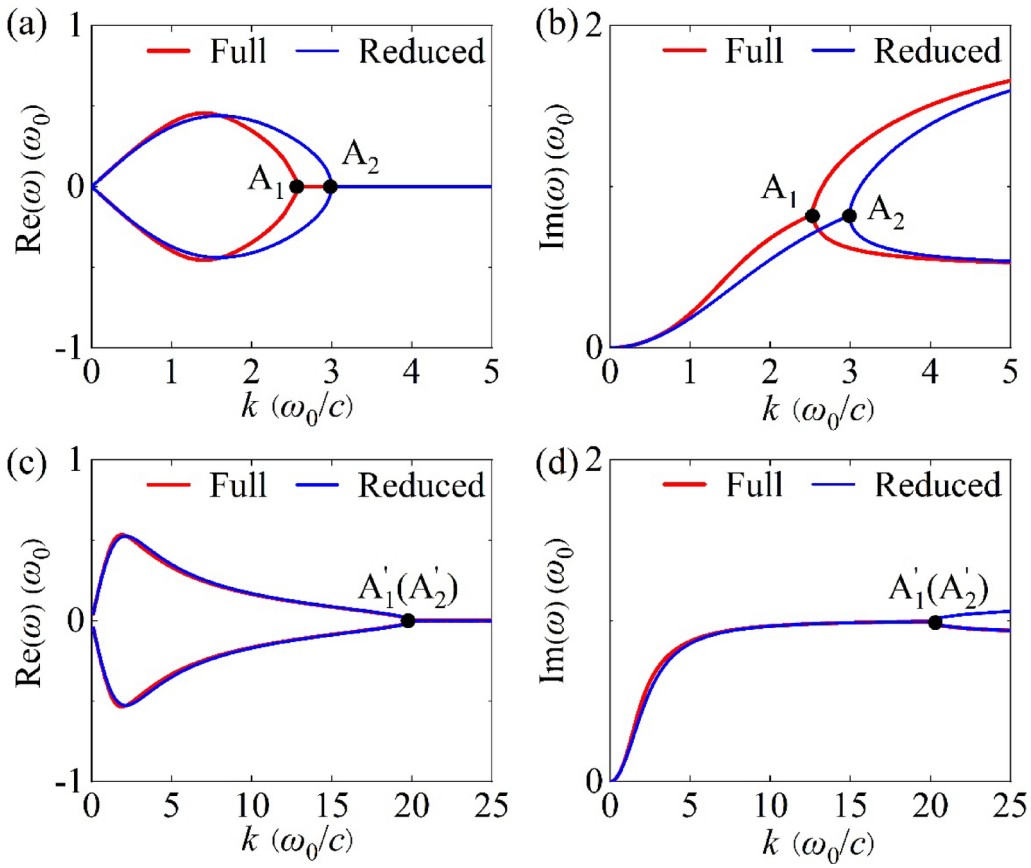

Fig. 4. (**a**) The real and (**b**) the imaginary parts of band dispersions obtained by the full (red) and the reduced Hamiltonians (blue), with $\omega_p = 2\omega_0$ and $\gamma = 2.5\omega_0$. EPs A_1 and A_2 are located at $k = 2.6\omega_0/c$ and $k = 3\omega_0/c$, respectively. (**c**) Real and (**d**) imaginary parts of band dispersions obtained correspondingly, with $\omega_p = 2\omega_0$. Both EPs A_1' and A_2' emerge at $k = 20\omega_0/c, \gamma = 2.01\omega_0$.

reduced Hamiltonian deviates from the rigorous results obtained from the full Hamiltonian. However, both Hamiltonians predict the existence of EP in the band diagram. Moreover, although the location of EP in the wavenumber is slightly shifted, the frequency of EP is accurately produced by the reduced Hamiltonian.

We note that the discrepancy between the two results can be further reduced by optimizing the values of k and γ, such that $\tilde{\omega}_{3,4}$ are significantly separated from $\tilde{\omega}_{1,2}$. Here, we let $\gamma \to 2\omega_0$, such that $\tilde{\omega}_1$ and $\tilde{\omega}_2$ coalesce and form an EP2 at $k \to \infty$. Around this EP2, the eigenfrequencies are given by

$$\lim_{k\to\infty} \tilde{\omega}_1 = \frac{i\left(\gamma - \sqrt{\gamma^2 - 4\omega_0^2}\right)}{2}, \tag{23a}$$

$$\lim_{k\to\infty} \tilde{\omega}_2 = \frac{i\left(\gamma + \sqrt{\gamma^2 - 4\omega_0^2}\right)}{2}, \tag{23b}$$

$$\lim_{k\to\infty} \tilde{\omega}_3 = -\infty, \tag{23c}$$

$$\lim_{k\to\infty} \tilde{\omega}_4 = \infty. \tag{23d}$$

From Eq. (23), it is straightforward that $\tilde{\omega}_{3,4} \gg \tilde{\omega}_{1,2}$. As shown in the Fig. 4c–d, the band dispersions obtained by the full and reduced Hamiltonian accord with each other very well when we choose $\gamma = 2.01\omega_0$. And an EP2 occurs at a large k ($20\omega_0/c$). The bands for $\tilde{\omega}_{3,4}$ are not shown because they are too large in their magnitudes.

However, we should note that when the four eigenfrequencies are in close proximity, their mutual couplings cannot be neglected, such as the region around the EP4. In this scenario, the use of 2×2 reduced Hamiltonian will introduce significant errors.

We note that the formulated Hamiltonian can also be used for calculating the Green's function, which serves as a powerful tool for the eigenmode retrieval[4]. In our case, the dyadic Green's function is calculated according to[4,46]:

$$\overleftrightarrow{G}(\omega) = \sum_{i=1}^{4} \frac{\vec{\psi}_i \vec{\psi}_i^L}{\sqrt{|\vec{\psi}_i|^2 |\vec{\psi}_i^L|^2}(\omega - \tilde{\omega}_i)}, \tag{24}$$

where $\vec{\psi}_i^L$ is the left eigenvector of $\hat{H}$ obtained by:

$$\vec{\psi}_i^L \hat{H} = \vec{\psi}_i^L \tilde{\omega}_i. \tag{25}$$

Lastly, to advance future research, we propose a possible experimental proposal. Experimentally, a feasible implementation of Lorentz dispersive media can be achieved by utilizing lattices of metallic split-ring resonators (SRRs) and rods[47,48]. The plasmon frequency ω_p can be finely adjusted by varying the filling ratios of SRRs to the background medium, and the damping rate γ can be modulated by modifying the lumped resistors placed at the outer corners of the SRRs. Notably, by increasing the resistances of the resistors, the damping rate can be much larger than the resonant frequency and in principle exceed $4\omega_0$, enabling the observations of ELs and EP4. However, since the medium exhibits loss, the exceptional lines (ELs) and higher-order exceptional points (EPs) are generally located in the complex frequency plane. Therefore, to excite the eigenstates at these ELs and higher-order EPs, beams with complex frequencies[49] must be used.

Conclusions

In conclusion, we theoretically investigate the realization of ELs and EP4 in the band diagrams of a space-time invariant Lorentz dispersive medium exhibiting uniform loss. We reveal that uniform loss in the Lorentz dispersive medium induces non-Hermitian couplings between the eigenmodes of the lossless system, offering a distinctive pathway to EPs distinct from conventional approaches relying on differential loss/gain engineering. Furthermore, we find that the electromagnetic field exhibits peak optical chirality density at the EP4. Last but not least, while our study focuses on the photonic system, the theoretical framework can be readily extended to other physical systems exhibiting Lorentz-type resonances.

Data availability

Data availabilityThe data in this study are available from the authors upon reasonable request.

Received: 31 January 2025; Accepted: 2 May 2025
Published online: 10 May 2025

References

1. El-Ganainy, R. et al. Non-Hermitian physics and PT symmetry. *Nat. Phys.* **14**, 11–19. https://doi.org/10.1038/nphys4323 (2018).
2. Bender, C. M. & Hook, D. W. PT-symmetric quantum mechanics. *Rev. Mod. Phys.* **96** https://doi.org/10.1103/RevModPhys.96.045002 (2024).
3. Rotter, I. A non-Hermitian Hamilton operator and the physics of open quantum systems. *J. Phys. A: Math. Theor.* **42** https://doi.org/10.1088/1751-8113/42/15/153001 (2009).
4. Ding, K., Ma, G., Xiao, M., Zhang, Z. Q. & Chan, C. T. Emergence, coalescence, and topological properties of multiple exceptional points and their experimental realization. *Phys. Rev. X* **6** https://doi.org/10.1103/PhysRevX.6.021007 (2016).
5. Shi, C. et al. Accessing the exceptional points of parity-time symmetric acoustics. *Nat. Commun.* **7**, 11110. https://doi.org/10.1038/ncomms11110 (2016).
6. Tang, W. et al. Exceptional nexus with a hybrid topological invariant. *Science* **370**, 1077–1080. https://doi.org/10.1126/science.abd8872 (2020).
7. Fang, X. et al. Observation of higher-order exceptional points in a non-local acoustic metagrating. *Commun. Phys.* **4** https://doi.org/10.1038/s42005-021-00779-x (2021).
8. Liu, T., Zhu, X., Chen, F., Liang, S. & Zhu, J. Unidirectional wave vector manipulation in two-dimensional space with an all passive acoustic parity-time-symmetric metamaterials crystal. *Phys. Rev. Lett.* **120**, 124502. https://doi.org/10.1103/PhysRevLett.120.124502 (2018).
9. Choi, Y., Hahn, C., Yoon, J. W. & Song, S. H. Observation of an anti-PT-symmetric exceptional point and energy-difference conserving dynamics in electrical circuit resonators. *Nat. Commun.* **9**, 2182. https://doi.org/10.1038/s41467-018-04690-y (2018).
10. Kazemi, H., Nada, M. Y., Mealy, T., Abdelshafy, A. F. & Capolino, F. Exceptional points of degeneracy induced by linear Time-Periodic variation. *Phys. Rev. Appl.* **11** https://doi.org/10.1103/PhysRevApplied.11.014007 (2019).
11. Regensburger, A. et al. Parity–time synthetic photonic lattices. *Nature* **488**, 167–171. https://doi.org/10.1038/nature11298 (2012).
12. Zyablovsky, A. A., Vinogradov, A. P., Pukhov, A. A., Dorofeenko, A. V. & Lisyansky, A. A. PT-symmetry in optics. *Phys. Usp.* **57**, 1063–1082. https://doi.org/10.3367/UFNe.0184.201411b.1177 (2014).
13. Miri, M. A. & Alu, A. Exceptional points in optics and photonics. *Science* **363** https://doi.org/10.1126/science.aar7709 (2019).
14. Ozdemir, S. K., Rotter, S., Nori, F. & Yang, L. Parity-time symmetry and exceptional points in photonics. *Nat. Mater.* **18**, 783–798. https://doi.org/10.1038/s41563-019-0304-9 (2019).
15. Koutserimpas, T. T. & Fleury, R. Electromagnetic fields in a Time-Varying medium: Exceptional points and operator symmetries. *IEEE Trans. Antennas Propag.* **68**, 6717–6724. https://doi.org/10.1109/tap.2020.2996822 (2020).
16. Wang, C., Sweeney, W. R., Stone, A. D. & Yang, L. Coherent perfect absorption at an exceptional point. *Science* **373**, 1261–1265. https://doi.org/10.1126/science.abj1028 (2021).
17. Li, A. et al. Exceptional points and non-Hermitian photonics at the nanoscale. *Nat. Nanotechnol.* **18**, 706–720. https://doi.org/10.1038/s41565-023-01408-0 (2023).
18. Liu, W. et al. Floquet parity-time symmetry in integrated photonics. *Nat. Commun.* **15**, 946. https://doi.org/10.1038/s41467-024-45226-x (2024).
19. Feng, L., Wong, Z. J., Ma, R. M., Wang, Y. & Zhang, X. Single-mode laser by parity-time symmetry breaking. *Science* **346**, 972–975. https://doi.org/10.1126/science.1258479 (2014).
20. Gao, X., He, H., Sobolewski, S., Cerjan, A. & Hsu, C. W. Dynamic gain and frequency comb formation in exceptional-point lasers. *Nat. Commun.* **15**, 8618. https://doi.org/10.1038/s41467-024-52957-4 (2024).
21. Xu, H., Mason, D., Jiang, L. & Harris, J. G. Topological energy transfer in an optomechanical system with exceptional points. *Nature* **537**, 80–83. https://doi.org/10.1038/nature18604 (2016).

22. Weidemann, S. et al. Topological funneling of light. *Science* **368**, 311–314. https://doi.org/10.1126/science.aaz8727 (2020).
23. Bergholtz, E. J., Budich, J. C. & Kunst, F. K. Exceptional topology of non-Hermitian systems. *Rev. Mod. Phys.* **93** https://doi.org/10.1103/RevModPhys.93.015005 (2021).
24. Zhang, R. Y., Cui, X., Chen, W. J., Zhang, Z. Q. & Chan, C. T. Symmetry-protected topological exceptional chains in non-Hermitian crystals. *Commun. Phys.* **6** https://doi.org/10.1038/s42005-023-01291-0 (2023).
25. Zhang, X., Zangeneh-Nejad, F., Chen, Z. G., Lu, M. H. & Christensen, J. A second wave of topological phenomena in photonics and acoustics. *Nature* **618**, 687–697. https://doi.org/10.1038/s41586-023-06163-9 (2023).
26. Chen, W., Ozdemir, K., Zhao, S., Wiersig, G., Yang, L. & J. & Exceptional points enhance sensing in an optical microcavity. *Nature* **548**, 192–196. https://doi.org/10.1038/nature23281 (2017).
27. Klaiman, S., Günther, U. & Moiseyev, N. Visualization of branch points inPT-Symmetric waveguides. *Phys. Rev. Lett.* **101** https://doi.org/10.1103/PhysRevLett.101.080402 (2008).
28. Makris, K. G., El-Ganainy, R., Christodoulides, D. N. & Musslimani, Z. H. Beam dynamics in PT symmetric optical lattices. *Phys. Rev. Lett.* **100**, 103904. https://doi.org/10.1103/PhysRevLett.100.103904 (2008).
29. Longhi, S. Bloch oscillations in complex crystals with PT symmetry. *Phys. Rev. Lett.* **103**, 123601. https://doi.org/10.1103/PhysRevLett.103.123601 (2009).
30. Rüter, C. E. et al. Observation of parity–time symmetry in optics. *Nat. Phys.* **6**, 192–195. https://doi.org/10.1038/nphys1515 (2010).
31. Guo, A. et al. Observation of PT-symmetry breaking in complex optical potentials. *Phys. Rev. Lett.* **103**, 093902. https://doi.org/10.1103/PhysRevLett.103.093902 (2009).
32. Yang, X. et al. Observation of transient Parity-Time symmetry in electronic systems. *Phys. Rev. Lett.* **128**, 065701. https://doi.org/10.1103/PhysRevLett.128.065701 (2022).
33. Hodaei, H. et al. Enhanced sensitivity at higher-order exceptional points. *Nature* **548**, 187–191. https://doi.org/10.1038/nature23280 (2017).
34. Wang, S. et al. Arbitrary order exceptional point induced by photonic spin-orbit interaction in coupled resonators. *Nat. Commun.* **10**, 832. https://doi.org/10.1038/s41467-019-08826-6 (2019).
35. Zhang, G. Q. & You, J. Q. Higher-order exceptional point in a cavity magnonics system. *Phys. Rev. B* **99**, 054404. https://doi.org/10.1103/PhysRevB.99.054404 (2019).
36. Zhong, Q., Kou, J., Özdemir, Ş. K. & El-Ganainy, R. Hierarchical construction of Higher-Order exceptional points. *Phys. Rev. Lett.* **125**, 203602. https://doi.org/10.1103/PhysRevLett.125.203602 (2020).
37. Habler, N. & Scheuer, J. Higher-order exceptional points: A route for flat-top optical filters. *Phys. Rev. A*. **101** https://doi.org/10.1103/PhysRevA.101.043828 (2020).
38. Ding, K., Fang, C. & Ma, G. Non-Hermitian topology and exceptional-point geometries. *Nat. Reviews Phys.* **4**, 745–760. https://doi.org/10.1038/s42254-022-00516-5 (2022).
39. Wang, N., Hong, B. & Wang, G. P. Higher-order exceptional points and enhanced polarization sensitivity in anisotropic photonic time-Floquet crystals. *Opt. Express*. **32** https://doi.org/10.1364/oe.539505 (2024).
40. Yulaev, A. et al. Exceptional points in lossy media lead to deep polynomial wave penetration with spatially uniform power loss. *Nat. Nanotechnol.* **17**, 583–589. https://doi.org/10.1038/s41565-022-01114-3 (2022).
41. Raman, A. & Fan, S. Photonic band structure of dispersive metamaterials formulated as a Hermitian eigenvalue problem. *Phys. Rev. Lett.* **104**, 087401. https://doi.org/10.1103/PhysRevLett.104.087401 (2010).
42. Lalanne, P., Yan, W., Vynck, K., Sauvan, C. & Hugonin, J. P. Light interaction with photonic and plasmonic resonances. *Laser Photonics Rev.* **12** https://doi.org/10.1002/lpor.201700113 (2018).
43. Mun, J. et al. Electromagnetic chirality: From fundamentals to nontraditional chiroptical phenomena. *Light Sci. Appl.* **9**, 139. https://doi.org/10.1038/s41377-020-00367-8 (2020).
44. Tang, Y. & Cohen, A. E. Optical chirality and its interaction with matter. *Phys. Rev. Lett.* **104**, 163901. https://doi.org/10.1103/PhysRevLett.104.163901 (2010).
45. Poulikakos, L. V. et al. Optical chirality flux as a useful Far-Field probe of chiral near fields. *ACS Photonics*. **3**, 1619–1625. https://doi.org/10.1021/acsphotonics.6b00201 (2016).
46. Arfken, G. B., Weber, H. J. & Harris, F. E. *Mathematical methods for physicists: a comprehensive guide*Academic press,. (2011).
47. Pendry, J. B., Holden, A. J., Robbins, D. J. & Stewart, W. J. Magnetism from conductors and enhanced nonlinear phenomena. *IEEE Trans. Microwave Theory Tech.* **47**, 2075–2084. https://doi.org/10.1109/22.798002 (1999).
48. Ye, D. et al. Ultrawideband dispersion control of a metamaterial surface for perfectly-matched-layer-like absorption. *Phys. Rev. Lett.* **111**, 187402. https://doi.org/10.1103/PhysRevLett.111.187402 (2013).
49. Guan, F. et al. Overcoming losses in superlenses with synthetic waves of complex frequency. *Science* **381**, 766–771 (2023).

Acknowledgements

This work is supported by Key Project of the National Key R D program of China (2022YFA1404500), and National Natural Science Foundation of China (NSFC) (No. 12074267, No. 12174263 and No. 62105213).

Author contributions

Neng Wang and GuoPing Wang conceived the idea. Fanghu Feng did the theoretical calculations, numerical simulations, and prepared the manuscript. Neng Wang and GuoPing Wang revised the manuscript and supervised the whole project.

Declarations

Competing interests

The authors declare no competing interests.

Additional information

Correspondence and requests for materials should be addressed to N.W. or G.P.W.

Reprints and permissions information is available at www.nature.com/reprints.

Publisher's note Springer Nature remains neutral with regard to jurisdictional claims in published maps and institutional affiliations.